INTERNATIONAL JOURNAL FOR NUMERICAL METHODS IN FLUIDS
*Int. J. Numer. Meth. Fluids* 2008; **57**:793–810
Published online 27 November 2007 in Wiley InterScience (www.interscience.wiley.com). DOI: 10.1002/fld.1659

# Numerical simulations of droplet formation in a cross-junction microchannel by the lattice Boltzmann method

Long Wu[1,*,†], Michihisa Tsutahara[1], LaeSung Kim[2] and ManYeong Ha[2]

[1]*Graduate School of Science and Technology, Kobe University, 1-1, Rokkodaicho Nada, Kobe 657-8501, Japan*
[2]*School of Mechanical Engineering, Pusan National University, San 30, Jangjeonn-Dong, Kumjung-Ku, Pusan 609-735, Korea*

SUMMARY

An immiscible liquid–liquid multiphase flow in a cross-junction microchannel was numerically studied using the lattice Boltzmann method. An improved, immiscible lattice BGK model was proposed by introducing surface tension force based on the continuum surface force (CSF) method. Recoloring step was replaced by the anti-diffusion scheme in the mixed region to reduce the side-effect and control the thickness of the interface. The present method was tested by the simulation of a static bubble. Laplace's law and spurious velocities were examined. The results show that our model is more advantageous for simulations of immiscible fluids than the existing immiscible lattice BGK models. Computational results of multiphase flow in a cross-junction microchannel were obtained and analyzed based on dimensionless numbers. It is found that the flow pattern is decided mostly by the capillary number at a small inlet flux. However, at the same capillary number, a large inlet flux will lead to much smaller droplet generation. For this case, the flow is determined by both the capillary number and the Weber number. Copyright © 2007 John Wiley & Sons, Ltd.

Received 30 November 2006; Revised 11 April 2007; Accepted 4 October 2007

KEY WORDS: immiscible fluids; lattice Boltzmann method; spurious velocity; surface tension; cross-junction microchannel

## 1. INTRODUCTION

Nowadays, miniaturized chemical reactors are widely used due to their high portability, reduced reagent consumption, minimization of waste production and excellent mass and heat transfer properties [1]. Some of these devices have already been used for catalyst screening tools and food, cosmetics and pharmaceutical products. Recently, immiscible liquid–liquid multiphase flows in microchannels have attracted extensive attention owing to the segmentation of the two fluids,

*Correspondence to: Long Wu, Graduate School of Science and Technology, Kobe University, 1-1, Rokkodaicho Nada, Kobe 657-8501, Japan.
†E-mail: wulong@kobe-u.ac.jp

whereby the chemical reaction, mixing and diffusion of the solutes can be enhanced greatly. On the other hand, microdroplets can be produced in such a liquid–liquid system in the microchannel under certain conditions. The efficiency for generating microdroplets and properties of the liquid–liquid flow in microchannels is mainly influenced by the channel geometry, viscosity, interfacial tension, the inlet flux of two liquids and so on. The various parameters involved mean that optimizing the liquid–liquid multiphase flow in microreactors requires extensive experimental work. Therefore, a numerical study on such a system is indispensable to provide a reasonable and economically designed process.

As is well known, the variety and complexity of multiphase flows pose major challenges to a modeling approach. Accurate simulation of multiphase flow problems with a moving interface requires obtaining a sharp interface and recovering surface tension, which is often quite difficult for computational fluid dynamics (CFD) researchers. Several techniques were developed in the past 25 years and can be classified into three main categories according to their physical and mathematical approaches: capturing (Lagrangian), tracking (Eulerian) and combined methods. Among the various approaches of multiphase flow simulation, volume-of-fluid (VOF) [2], level set method [3] and front-tracking method [4] are known as useful and popular tools. Further new developments on capturing the interface include the particle-mesh method [5], the CIP method [6], the LBM method [7] and so on.

For the simulation of multiphase flow in microchannels, although the mentioned CFD packages can provide a general description of droplet formation, simulations by traditional computation fluid dynamics are computationally expensive, partially due to interface-tracking costs. Another challenge is the combination of very low velocity and small capillary number $Ca$, which means that spurious velocities (present in most computational schemes) become comparable to the modeled flow velocity in magnitude. To overcome the difficulties mentioned above, the lattice Boltzmann method is employed in this study. An improved immiscible lattice BGK model is also proposed with the spurious velocities significantly reduced.

The objective of this study is to achieve a better understanding of droplet formation in a cross-junction microchannel. First, we proposed an improved immiscible fluid model based on the lattice Boltzmann method. Next, to test our code, Static bubble flows were simulated. The results were compared with those simulated by some existing models. Then, the simulations of droplet formation were performed and compared with experimental results. Finally, a dimensionless study was presented to illustrate the influence of the capillary number and Weber number on the final droplet size.

## 2. NUMERICAL METHOD

In this section, the original immiscible lattice BGK model (Gunstensen model [8]) is reviewed briefly and then two other improved versions are presented, including the Lishchuk model [9] and the Latva-Kokko model [10]; finally, a more reasonable variation is given in detail.

### *2.1. Existing models*

Gunstensen [8] reported the first immiscible lattice BGK model for multiphase flow. Two fluids denoted by different colors, red and blue, obey the lattice Boltzmann equation as

$$f_i^k(\mathbf{x}+\mathbf{e}_i, t+1) - f_i^k(\mathbf{x}, t) = \Omega_i^k(\mathbf{x}, t) \tag{1}$$



DOI: 10.1002/fld

where $f_i^k(\mathbf{x},t)$ is the particle distribution function in the $i$th velocity direction for the $k$th fluid (red or blue) at position $\mathbf{x}$ and time $t$. $\mathbf{e}_i$ is the particle velocity of the $i$th direction. These particle distribution functions evolve according to Equation (1). The collision operator, $\Omega_i^k(\mathbf{x},t)$, is split into two parts. The first part denoted by $(\Omega_i^k)^1$ is the same as the BGK single-phase collision term and can be simplified as

$$(\Omega_i^k)^1 = -\frac{1}{\tau_k}[f_i^k(\mathbf{x},t) - f_i^{k(\mathrm{eq})}(\mathbf{x},t)] \tag{2}$$

where $f_i^{k(\mathrm{eq})}(\mathbf{x},t)$ is the equilibrium distribution function at position $\mathbf{x}$ and time $t$, and $\tau_k$ is the single-relaxation time for the $k$th fluid. The second part of the collision operator (perturbation step) for the 2-D 7-speed model is given as [8]

$$(\Omega_i^k)^2 = A|\mathbf{G}|\cos 2(\theta_i - \theta_f) \tag{3}$$

where $A$ is the adjustable surface tension parameter, $\theta_i$ is the angle of lattice direction $i$ and $\theta_f$ is the angle of the local gradient of the color field $G$, which is defined as

$$\mathbf{G}(\mathbf{x},t) = \sum_i \mathbf{e}_i[\rho_{\mathrm{r}}(\mathbf{x}+\mathbf{e}_i,t) - \rho_{\mathrm{b}}(\mathbf{x}+\mathbf{e}_i,t)] \tag{4}$$

where $\rho_{\mathrm{r}}$ and $\rho_{\mathrm{b}}$ are densities of red and blue fluids. To prevent the two fluids from mixing with each other, the so-called recoloring step is applied. The basic idea of recoloring is to keep the sharpness of interface by reallocating $f_i^k(\mathbf{x},t)$ in the mixed region at the collision step, so that as few colored particles as possible cross the interface. The colored particles are demixed relative to the color field by maximizing the work done by the color flux $\mathbf{q}(\mathbf{x},t)$ [8],

$$\mathbf{q}(\mathbf{x},t) = \sum_i \mathbf{e}_i[f_i^{\mathrm{r}}(\mathbf{x},t) - f_i^{\mathrm{b}}(\mathbf{x},t)] \tag{5}$$

Because of this 'recolor' procedure, particles of each color tend to congregate together. Thus, the two fluids are forced to be immiscible.

Based on Gunstensen model, Lishchuk [9] modified the algorithm by replacing the perturbation step with a direct force term at the mixed region. This force term is used to recover the required pressure difference across the interface, which is known as Laplace's law. Lishchuk's approach is a very different process compared with Gunstensen's method. It builds up the inner pressure of the droplet through a net body force acting at the interface. This step causes the interfacial length to decrease slightly and also produces the desired surface tension. It has already been reported that Lishchuk's method provides much better drop isotropy and reduces spurious velocities significantly. This enhanced behavior is probably due to its second-order gradient quantities that make the surface tension less local than that in Gunstensen's method [9].

For Gunstensen's method, the recoloring step serves as an artificial anti-diffusion for separating the two phases by maximizing the work of the color flux in the original immiscible lattice BGK model. This kind of anti-diffusion has an adverse side effect at the interface, which makes the interface profile to be zigzag. This may be caused by the lack of diffusion along the interface. Thus, it is a natural idea to seek help in the replacement of the recoloring method with a moderate diffusion procedure. Recently, Latva-Kokko and Rothman [10] reported a new scheme for the recoloring step by introducing an adjustable parameter $\beta$, which controls the strength of phase diffusion. This model is discussed in detail in Section 2.2. Although Latva-Kokko's idea is used



DOI: 10.1002/fld

to fix the lattice pinning problem of the original immiscible lattice BGK model, its improvement can also be used for resolving the side-effect problem. It should also be noted that this improved recoloring step is much easier to implement than the old one (Gunstensen model). With the improved method, the distribution of red and blue particles is symmetric around the color gradient.

### *2.2. Our improved model*

Based on the above discussions, we modify the Gunstensen model by replacing the perturbation step with a direct force term at the mixed region (interface) and change the recoloring step by including moderate diffusion along the interface.

With the same notations, the lattice Boltzmann equation for the $k$th component can be expressed in the same form as Equation (1), with the collision term being

$$\Omega_i^k(\mathbf{x},t) = -\frac{1}{\tau_k}[f_i^k(\mathbf{x},t) - f_i^{k(\mathrm{eq})}(\mathbf{x},t)] \tag{6}$$

The 2-D 9-speed square lattice is chosen in the present method, so that a suitable equilibrium distribution function takes the form

$$f_i^{k(\mathrm{eq})} = w_i \rho^k (1 + 3e_{i\alpha}u_\alpha + \tfrac{9}{2}e_{i\alpha}e_{i\beta}u_\alpha u_\beta - \tfrac{3}{2}\mathbf{u}^2) \tag{7}$$

with $w_0 = \frac{4}{9}$, $w_i = \frac{1}{9}$ for $i = 1, 2, 3, 4$, $w_i = \frac{1}{36}$ for $i = 5, 6, 7, 8$.

In Equation (6), $\tau_k$ is the relaxation time for each kind of fluid. It is also used to decide the value of kinematic viscosity as

$$\nu = \frac{2\tau - 1}{6} \tag{8}$$

where $\tau$ is the relaxation time for the color blind fluid and is defined as $\tau = \sum \rho^k \tau_k / \rho$. These collision and relaxation rules lead to the following macroscopic mass and momentum equations [11] as:

$$\partial_t \rho + \nabla \cdot (\rho \mathbf{u}) = 0 \tag{9}$$

$$\partial_t \mathbf{u} + \mathbf{u} \cdot \nabla \mathbf{u} = -\frac{1}{\rho}\nabla p + \nu \nabla^2 \mathbf{u} \tag{10}$$

The densities $\rho^k$ for different phases, the total density $\rho$, momentum $\rho\mathbf{u}$ and pressure $p$ are obtained from the following equations:

$$\rho^k = \sum_{i=0}^{8} f_i^k = \sum_{i=0}^{8} f_i^{k(\mathrm{eq})} \tag{11}$$

$$\rho = \sum_k \rho^k \tag{12}$$

$$\rho\mathbf{u} = \sum_{i=0}^{8} \mathbf{e}_i f_i = \sum_{i=0}^{8} \mathbf{e}_i f_i^{\mathrm{eq}} \tag{13}$$

$$p = \tfrac{1}{3}\rho \tag{14}$$



DOI: 10.1002/fld

In order to recover the surface tension effect, a local pressure gradient across the interface is forced by an additional force term. A popular model for the interfacial tension force is the continuum surface force (CSF) model, which was developed by Brackbill *et al.* in 1992 [12]. In the CSF model the interfacial tension was interpreted as a continuous 3-D effect across an interface rather than as a pressure boundary condition on the interface. It is used in our multiphase simulation due to its easy implementation and high accuracy. After applying the surface tension force, the equilibrium distribution functions are the same as the ones given in Equation (7) except the velocity $\mathbf{u}$ is replaced by the equilibrium velocity $\mathbf{u}^{\mathrm{eq}}$, which is defined by the following relation:

$$\rho\mathbf{u}^{\mathrm{eq}} = \rho\mathbf{u} + \tau\mathbf{F} \tag{15}$$

The surface tension force $\mathbf{F}$ is added to the common velocity $\mathbf{u}$ and modeled as follows [12]:

$$\mathbf{F} = \sigma\kappa\frac{\nabla C}{|\nabla C|} \tag{16}$$

where $\sigma$ is the surface tension coefficient. The color field $C(\mathbf{x}, t)$ and interface curvature $\kappa$ are given as

$$C(\mathbf{x}, t) = \rho_{\mathrm{r}}(\mathbf{x}, t) - \rho_{\mathrm{b}}(\mathbf{x}, t) \tag{17}$$

$$\kappa = -(\nabla\cdot\hat{\mathbf{n}}) = \frac{1}{|\mathbf{n}|}\left[\left(\frac{\mathbf{n}}{|\mathbf{n}|}\cdot\nabla\right)|\mathbf{n}| - (\nabla\cdot\mathbf{n})\right] \tag{18}$$

where $\hat{\mathbf{n}}(\mathbf{x})$ is the unit normal to the interface and $\hat{\mathbf{n}}(\mathbf{x}) = \mathbf{n}(\mathbf{x})/|\mathbf{n}(\mathbf{x})|$. The normal vector $\mathbf{n}(\mathbf{x})$ is defined as

$$\mathbf{n}(\mathbf{x}) = \nabla C(\mathbf{x}) \tag{19}$$

The two parts inside the bracket of Equation (18) can be calculated as follows:

$$\begin{aligned}(\nabla\cdot\mathbf{n})_{i,j} &= \left(\frac{\partial n_x}{\partial x}\right)_{i,j} + \left(\frac{\partial n_y}{\partial y}\right)_{i,j} \\ &= \frac{1}{2\Delta x}[n_{x,i+1/2,j+1/2} + n_{x,i+1/2,j-1/2} - n_{x,i-1/2,j+1/2} - n_{x,i-1/2,j-1/2}] \\ &\quad + \frac{1}{2\Delta y}[n_{y,i+1/2,j+1/2} + n_{y,i-1/2,j+1/2} - n_{y,i+1/2,j-1/2} - n_{y,i-1/2,j-1/2}]\end{aligned} \tag{20}$$

$$\left(\frac{\mathbf{n}_{i,j}}{|\mathbf{n}_{i,j}|}\cdot\nabla\right)|\mathbf{n}| = \left(\frac{n_x}{|\mathbf{n}|}\right)_{i,j}\left(\frac{\partial|\mathbf{n}|}{\partial x}\right)_{i,j} + \left(\frac{n_y}{|\mathbf{n}|}\right)_{i,j}\left(\frac{\partial|\mathbf{n}|}{\partial y}\right)_{i,j} \tag{21}$$



DOI: 10.1002/fld

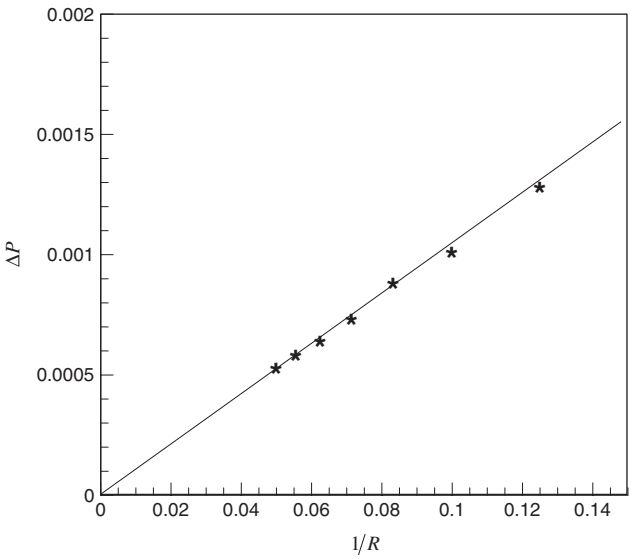


Figure 1. Numerical confirmation of Laplace's law by the present method.

The normal vector $\mathbf{n}_{i,j}$ on the grid point and cell-centered vector $\mathbf{n}_{i+1/2,j+1/2}$ are calculated by the following equations:

$$\mathbf{n}_{i,j} = \tfrac{1}{4}(\mathbf{n}_{i+1/2,j+1/2} + \mathbf{n}_{i+1/2,j-1/2} + \mathbf{n}_{i-1/2,j+1/2} + \mathbf{n}_{i-1/2,j-1/2}) \tag{22}$$

$$\mathbf{n}_{i+1/2,j+1/2} = \hat{\mathbf{x}}\left(\frac{C_{i+1,j} + C_{i+1,j+1} - C_{i,j} - C_{i,j+1}}{2\Delta x}\right) + \hat{\mathbf{y}}\left(\frac{C_{i,j+1} + C_{i+1,j+1} - C_{i,j} - C_{i+1,j}}{2\Delta y}\right) \tag{23}$$

The other improvement in our model is the modification of the recoloring step by implementing Latva-Kokko's diffusion scheme. The crucial part of this solution is to allow the red and the blue fluid to moderately mix along the interface and to keep the color distribution symmetric with respect to the color gradient. We use the following redistributions for the red and blue particles after the collision step:

$$f_i^{\mathrm{r}} = \frac{\rho_{\mathrm{r}}}{\rho_{\mathrm{r}} + \rho_{\mathrm{b}}} f_i + \beta \frac{\rho_{\mathrm{r}}\rho_{\mathrm{b}}}{(\rho_{\mathrm{r}} + \rho_{\mathrm{b}})^2} f_i^{\mathrm{eq}(0)} \cos\varphi \tag{24}$$

$$f_i^{\mathrm{b}} = \frac{\rho_{\mathrm{b}}}{\rho_{\mathrm{r}} + \rho_{\mathrm{b}}} f_i - \beta \frac{\rho_{\mathrm{r}}\rho_{\mathrm{b}}}{(\rho_{\mathrm{r}} + \rho_{\mathrm{b}})^2} f_i^{\mathrm{eq}(0)} \cos\varphi \tag{25}$$

where $f_i$ and $f_i^{\mathrm{eq}(0)}$ are the color blind distribution functions and zero-velocity equilibrium distribution functions going to the $i$th direction, respectively. $\varphi$, defined in Equation (26), is the angle between the color gradient and the particle velocities $\mathbf{e}_i$. $\beta$ is the parameter relating to the tendency



DOI: 10.1002/fld

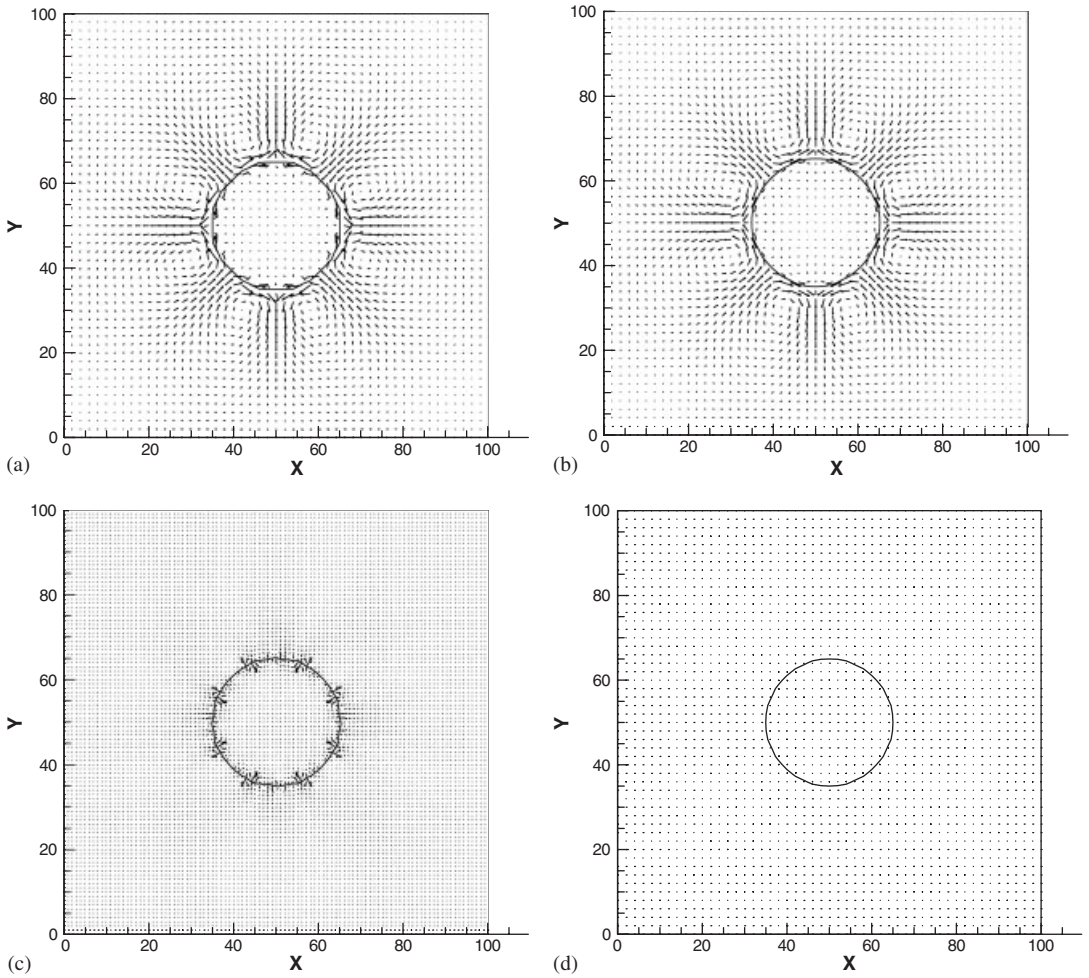


Figure 2. The distribution of velocity vectors for different models with surface tension being $\sigma = 0.001$. (a) Gunstensen's original two-color model, (b) Latva-Kokko's two-color model with diffusion, (c) Lishchuk's two-color model with surface tension based on continuum physics, and (d) Present model with surface tension based on continuum physics and Latva-Kokko's scheme.

of the two fluids to separate

$$\cos\varphi|_i = \frac{\mathbf{G}\cdot\mathbf{e}_i}{|\mathbf{G}||\mathbf{e}_i|} \tag{26}$$

where $\mathbf{G}$ is the local gradient of the color field with the same definition as given in Equation (4). Without the last term in Equations (24) and (25), red and blue particles would be distributed according to their numbers and there would be no tendency for separation of the two fluids. Here, $\beta$ can take any value between 0 and 1 to control the diffusion and width of the interface. When $\beta$ is larger than 1, there can be negative populations of particles, but if the negative values are kept



DOI: 10.1002/fld

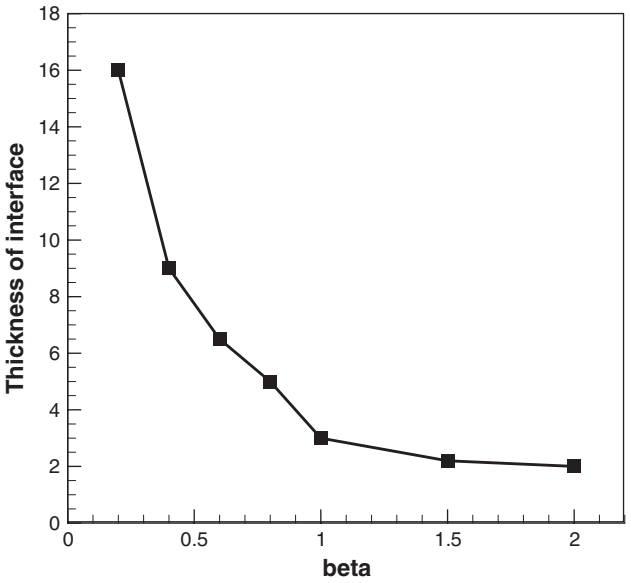


Figure 3. The thickness of the interface against various values of $\beta$.

small, the stability is maintained [10]. The relationship between the thickness of the interface and $\beta$ is discussed in the following section.

### *2.3. The advantage of current model*

The usefulness of our new model is demonstrated for easily and accurately simulating multiphase flow by the case of a static circular bubble with radius $R$. A 2-D (in the $xy$-plane) simulation is performed in a $100 \times 100$ lattice cell system, and the periodic boundary conditions are employed.

First, we test Laplace's law, which is given as

$$\Delta P = P_{\text{in}} - P_{\text{out}} = \sigma / R \tag{27}$$

where $P_{\text{in}}$ and $P_{\text{out}}$ are the average pressures inside and outside the bubble, respectively. Simulations with different initial bubble radii are performed, and the final radius $R$ and the pressure differences are recorded. Figure 1 is the plot of $\Delta P = P_{\text{in}} - P_{\text{out}}$ *versus* $1/R$. The value of $\sigma$ used for the test of Laplace's law is set to be 0.001. In Figure 1, all points representing a radius from 8 to 20 almost fit a straight line. The pressure difference inside and outside the bubble is indeed proportional to the reciprocal of the radius for our simulations. This test shows that our method can correctly model the surface tension effect.

Secondly, the spurious velocities are investigated for all the models discussed in Section 2.1. Figure 2(a)–(d) shows velocity vector plots in the final stage of bubble evolution for various models. The surface tension coefficient $\sigma = 0.001$ and the initial bubble radius $R = 15$ are chosen in these cases. Although there may be some small relative fluctuations as time evolves, they present the typical behavior of the velocity field. The magnitude of the velocity is represented by the length of the velocity vectors that have the same scale for all the models. The non-zero velocity fields in these figures represent the deviation of the results from the physical problem, especially



DOI: 10.1002/fld

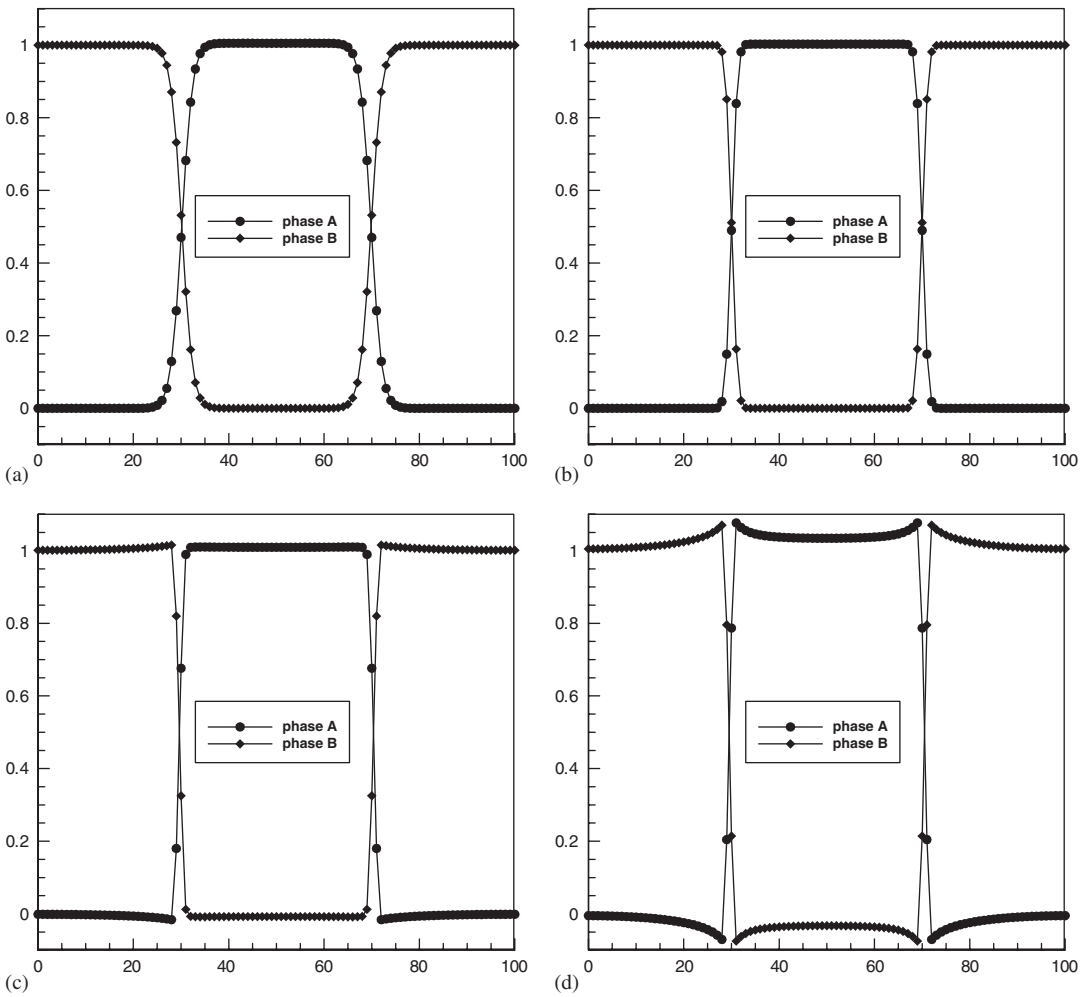


Figure 4. The interface profiles at various values of $\beta$: (a) $\beta=0.5$; (b) $\beta=1.0$; (c) $\beta=1.5$; and (d) $\beta=2.0$.

the velocities near the interface region. These non-zero velocities are called spurious velocities. For these cases shown in Figure 2(a)–(d), the spurious velocities are much more serious in the Gunstensen (a) and Latva-Kokko (b) models (based on the perturbation step method) than those in the Lishchuk (c) and present models (d) (based on direct surface tension force). The spurious velocities are closely related to the value of $A$ (in Equation (3)) in the perturbation-based model and can be reduced by using smaller values of $A$, but the surface tension decreases accordingly. In our model, the spurious velocities obtained under the same conditions appear to be much smaller. Furthermore, our model provides much better results than the Lishchuk model near the interface, which is because the side effect has been reduced greatly by introducing moderate diffusion.

Finally, the thickness of the interface and its dependence on the parameter $\beta$ (see Equations (24) and (25)) are examined for the current model. The surface tension coefficient $\sigma=0.001$ and the



DOI: 10.1002/fld

initial bubble radius $R=20$ are used here. Figure 3 shows the thickness of the interface against $\beta$ along the horizontal line at the middle of the computational area ($y=50$). From Figure 3, we can find that the thickness of the interface decreases significantly with the increase in the value of $\beta$. A very sharp interface can be obtained at large $\beta$. Figure 4 shows the interface profiles at various values of $\beta$. Four typical values of $\beta$ (0.5, 1.0, 1.5, 2.0) are used for discussion. When $\beta<1$ (Figure 4(a)), the interface profiles are very smooth but not so sharp. When $\beta\geqslant 1$ (Figure 4(b)–(d)), the profiles become sharper than that at small value of $\beta$. The thickness of the interface can be decreased effectively by increasing the value of $\beta$. Generally, it is better to control the interface as sharp as possible, but when the interface becomes very sharp, minus density distribution (negative population of particles) will occur near the interface as shown in Figure 4(c) and (d) ($\beta>1$). Besides, when $\beta>1$, the sharpness cannot be improved efficiently by increasing $\beta$ (see Figure 3). Also, the minus density distribution becomes significant at large $\beta$. This may lead to some very unreasonable results, since the density distributions are usually used for computing the average properties at the interface. Based on the above discussion, a moderate value $\beta=1$ is used in the following study to obtain a sharp interface and prevent the minus density distribution.

## 3. EXPERIMENTAL SETUP AND COMPUTATIONAL MODEL SYSTEM ON THE DROPLET FORMATION IN A CROSS-JUNCTION MICROCHANNEL

### *3.1. Experimental setup*

A cross-junction microchannel with three inlet ports and single outlet was used in this study as shown in Figure 5. The widths of main and lateral channels are 200 μm and 100 μm, respectively. The depth is 100 μm for the whole channel (for experimental setup but not shown in Figure 5). Water phase (denoted as A here) was introduced from the inlet of main channel, and oil phase (denoted as B here) was injected from the inlet of one of the lateral channels. The other lateral channel was used as the inlet channel for the water or oil phase as the case may be (oil phase was used in this study. In the experiment, water with 3% PVA ($\mu_A=1.074\times10^{-2}$ Pa s and $\rho_A=1.03\times10^3$ kg m$^{-3}$) was used as the water phase. Freol ALPHA 10G ($\mu_B=2.441\times10^{-2}$ Pa s and $\rho_B=0.93\times10^3$ kg m$^{-3}$) was used as the oil phase. The interfacial tension is $\sigma=0.03$ N m$^{-1}$. The magnitudes of the average inlet velocities are designated as $u_A$ for the water and $u_B$ for the oil. The velocity ratio is defined as $\alpha=u_A/u_B$. The channel was made of PDMS (polydimethylsiloxane) and was bonded to a glass plate by means of the plasma treatment using the $O_2$ plasma asher.

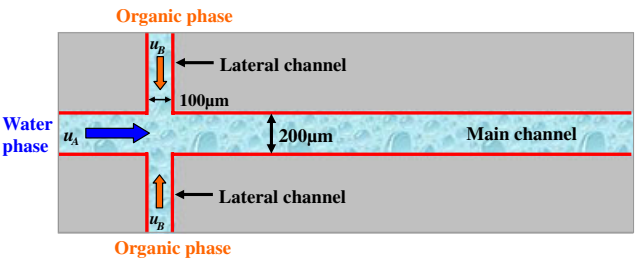


Figure 5. Model system for droplet formation in a cross-junction microchannel.



DOI: 10.1002/fld

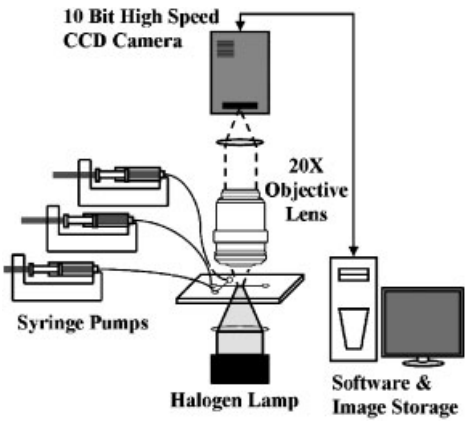


Figure 6. Schematic of the system setup. The micro-PIV system consists of a 10-bit high-speed CCD camera, a microscope and syringe pumps.

Figure 6 shows the schematic illustration of the experimental setup. The micro-PIV system consists of a 10-bit high-speed CCD camera (1200 h, PCO), a microscope (BX51, Olympus) and syringe pumps. A 10-bit high-speed CCD camera with a $1280 \times 1024$ pixel resolution was used to obtain time-resolved velocity fields as a microdroplet was formed. A halogen lamp was focused and illuminated to a test section from the bottom of the microchannel. Then, shadows of particles were formed on the image plane, unlike using fluorescent lights emitted from particles. Particles with 1 μm diameter were seeded into the working fluids: water-phase and oil-phase fluids. The particles contained in an aqueous solution were dried and mixed with the oil-phase fluid to seed the particles into the oil-phase fluid. Ultrasonic treatment and filtering were performed to disperse particles and eliminate lumps of several particles after mixing dried particles and the oil-phase fluid. To drive the flow, syringe-pumps were used.

### *3.2. Computational model system*

The 2-D computational model system is shown in Figure 5. The velocity and viscosity ratios are set to be $u_A/u_B = 1/6$ and $\lambda = \mu_A/\mu_B = 1$, respectively. Both phases are assumed to be incompressible, Newtonian and immiscible. The simulations are performed in a $300 \times 60$ cell system and each cell corresponds to 10 μm. This cell system was tested to be acceptable by comparing the results of a finer cell system of $600 \times 120$ (each cell size corresponds to 5 μm) in several different conditions. The relative error between the results of two cell systems is not more than 5%. No-slip boundary condition was applied for all the solid walls by the robust method of mid-link bounceback [13], which conveniently resolves the complex wall shapes and ensures the correct flux ratio by preventing the boundary 'leakage error' in small velocity cases. Inlet and outlet fluxes and an outlet pressure (density) distribution were specified at every time step using an appropriate equilibrium $f_i^{(0)}(\rho, \mathbf{u})$ [13].

Such flows are described by a large number of parameters including surface tension, variations in density, inlet velocity and viscosity across the two fluids. Luckily, several parameters are naturally small in this case. For instance, inertial effects are small compared with viscous effects, yielding small Reynolds numbers. Gravitational effects will also generally be small compared with surface



DOI: 10.1002/fld

tension, yielding a small Bond number. In contrast, the capillary number ($Ca$) always dominates the micro-flow, which describes the relative importance of viscosity and surface tension. The capillary number is defined as

$$Ca = \mu U / \sigma \tag{28}$$

where $\mu$ is the dynamic viscosity and set to be $\mu_A$ in this study, $U$ is a typical velocity and is chosen to be the average inlet velocity of fluid A ($u_A$) and $\sigma$ is the surface tension. Another important dimensionless parameter is the Weber number ($We$), which is defined as

$$We = \rho U^2 d / \sigma \tag{29}$$

with $\rho$ being a typical density and $d$ a length scale (the width of the main channel). The Weber number represents the comparison between inertial effects and surface tension effects. Although the length scales involved are small, the strong dependence on the velocity (squared term) can yield large values of $We$. This is particularly true when fluids are ejected from a nozzle at high speed, as in inkjet printing. Furthermore, several authors have reported the importance of the fluid interaction with the walls. In order to generate structures of one fluid (fluid A) within another (fluid B), fluid B (continuous phase) usually completely wets the walls of the microchannel while fluid A (to-be-dispersed phase) is non-wetting. In the following section, also concentrate on the case where only one fluid (fluid B) wets the walls. The same idea, as in Reference [14], is employed to recover the wetness effect.

## 4. RESULTS AND DISCUSSIONS

### *4.1. Comparison between simulation and experiment*

Figure 7 shows the process of droplet formation and the corresponding velocity fields obtained by our numerical simulation and experiment. The numerical conditions are $u_A = 0.0002$, $\mu_A = 0.1$ and $\sigma = 0.02$, corresponding to $Ca = 0.001$. Because the numerical and experimental conditions are not completely the same and there also exists some disagreement between the 2-D simulation and 3-D experiment, here only a qualitative comparison between simulation and experiment is made. First, from Figure 7 it can be found that the numerical results (droplet formation process and velocity field) agree very closely with the experimental results, which proves the ability of our model in simulating such a problem. Secondly, it can be seen that droplet formation proceeds in three stages, i.e. expansion (Figure 7(a)–(c)), necking (Figure 7(d)) and figuration (Figure 7(e)–(f)) stages. The final droplet size is a result of these three stages. From the velocity field, we can observe in the expansion stage (Figure 7(a)–(c)) that the velocity vectors are almost straightforward and no vortices appear. In the necking stage (Figure 7(d)), at the neck place, phase A is split suddenly to generate the droplet. This fast motion may be induced by strong surface tension forces, which increase rapidly with the sudden change in the curvature of the interface. In the figuration stage (Figure 7(e)), two symmetric vortices appear on the back of the generated droplet and on the front of the droplet that is subsequently generated. These vortices are desirable for some chemical reactions or mixing.



DOI: 10.1002/fld

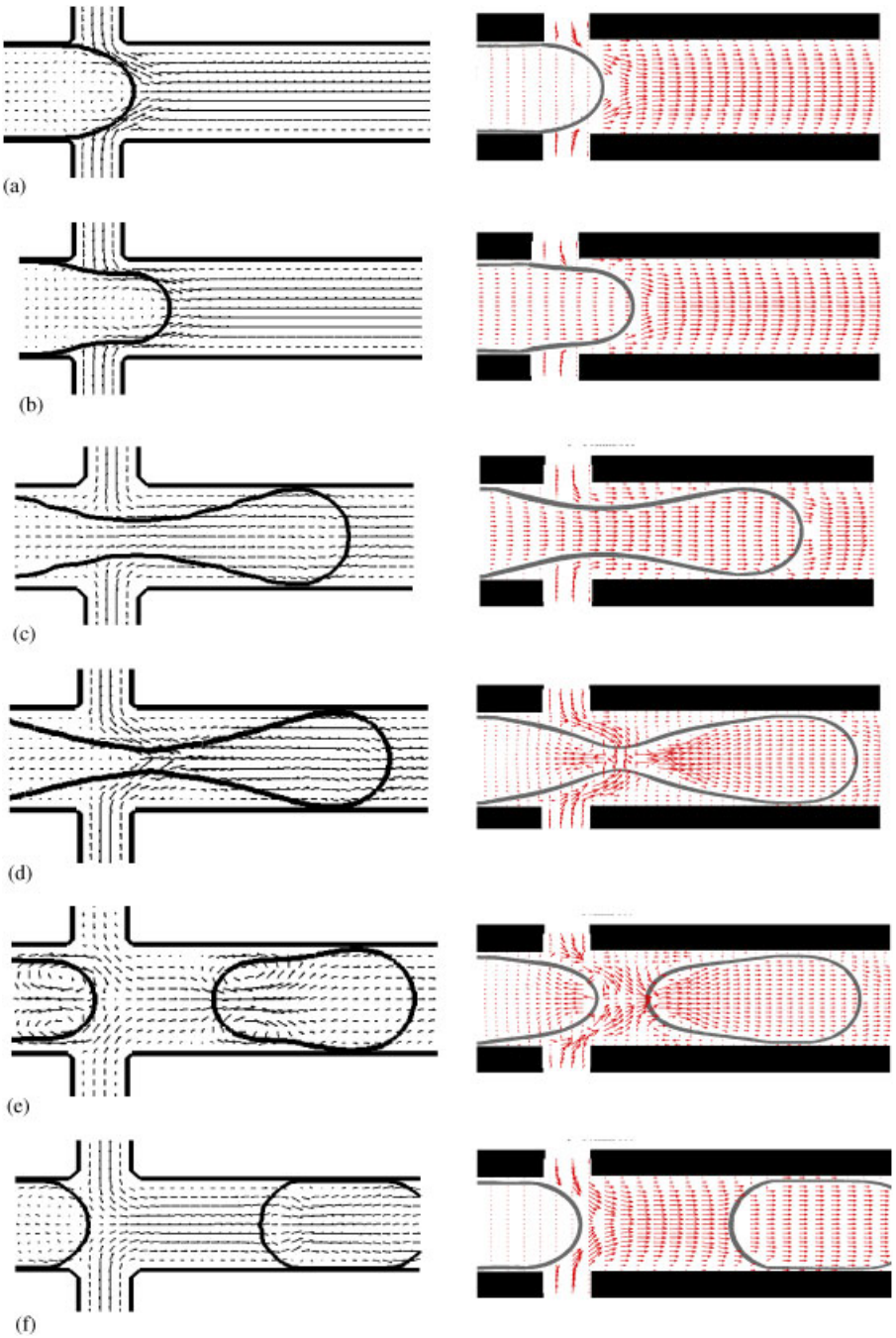


Figure 7. Comparisons between the current results (left) and experiment (right) for flow patterns and velocity vectors of different time steps: (a) 35 400; (b) 52 000; (c) 87 600; (d) 918 000; (e) 92 700; and (f) 98 400.



DOI: 10.1002/fld

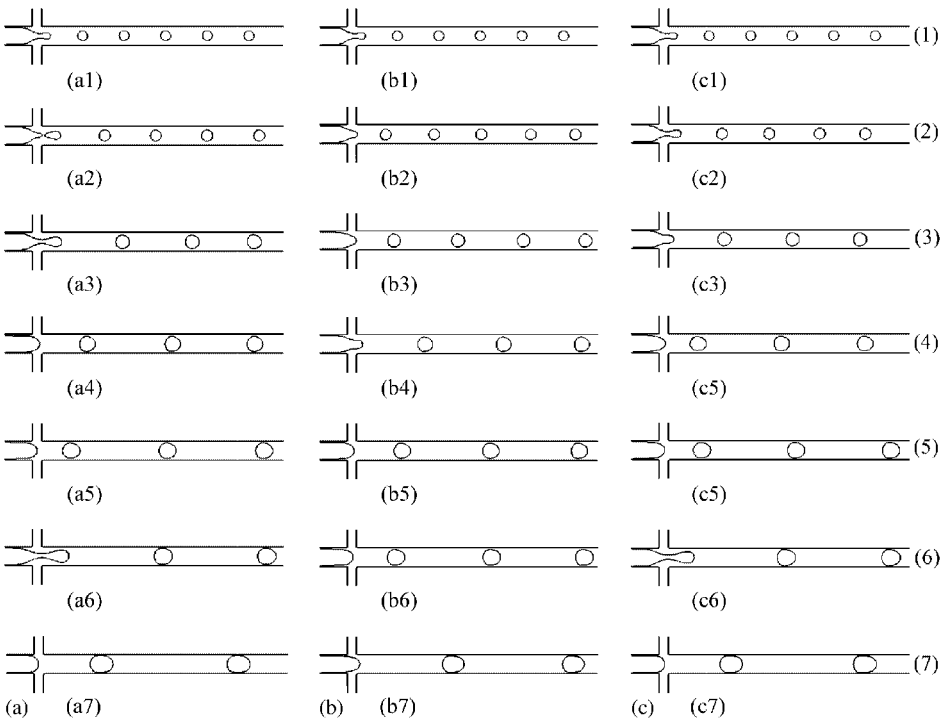


Figure 8. The flow patterns for various parameters, row for same *Ca*, column for single parameter changing, column (a) is for $u_A$ changing, column (b) is for $\mu_A$ changing, column (c) is for $\sigma$ changing (refer Table I for detailed conditions).

### *4.2. The influence of capillary number (Ca) and Weber number (We)*

A series of simulations are performed with various interfacial tensions $\sigma$ (0.008–0.08 N m$^{-1}$), dynamic viscosities $\mu_A$ (0.02–0.2 Pa s) and inlet velocities of the fluid A $u_A$ (0.0001–0.003 m s$^{-1}$), which are the main parameters appearing in both the capillary number and the Weber number.

Figure 8 shows the flow patterns for various *Ca*. Three parameters included in *Ca* (Equation (28)), i.e. inlet velocity (column a), viscosity (column b) and surface tension (column c), are studied individually by fixing the other two parameters. Detailed conditions are listed in Table I. From Figure 8, we find that the distance between two neighboring droplets increases with a decrease in *Ca* (from rows 1 to 7, *Ca* decrease). At the same time, the size of the generated droplets also increases when *Ca* decreases. At small *Ca*, the droplet diameter becomes larger than the width of the channel and slugs are generated (Figure 8, rows 4–7). On the contrary, at larger capillary number, the influence of the channel geometry decreases due to the smaller droplets generated, which do not touch the channel walls. For each row in Figure 8, at the same *Ca*, the shape and size of the droplets are almost the same, although the other dimensionless number *We* is different. This means that under the current conditions, the influence of *We* is much smaller than *Ca* and the flow pattern is decided by *Ca* predominantly. From the point of view of dimensionless analysis, decreasing $u_A$ (column a) and $\mu_A$ (column b) or increasing $\sigma$ (column c) leads to small *Ca*, which



DOI: 10.1002/fld

Table I. Corresponding parameters for Figures 8 and 9.

| | *Ca* | | | | | | |
|---|---|---|---|---|---|---|---|
| Parameters | 0.025 (1) | 0.02 (2) | 0.0125 (3) | 0.00833 (4) | 0.00625 (5) | 0.005 (6) | 0.002 (7) |
| $u_A =$ $\mu_A = 0.2$ $\sigma = 0.008$ | 0.001 (a1) | 0.0008 (a2) | 0.0005 (a3) | 0.00033 (a4) | 0.00025 (a5) | 0.0002 (a6) | 0.0001 (a7) |
| $u_A = 0.001$ $\mu_A =$ $\sigma = 0.008$ | 0.2 (b1) | 0.16 (b2) | 0.1 (b3) | 0.0667 (b4) | 0.05 (b5) | 0.04 (b6) | 0.02 (b7) |
| $u_A = 0.001$ $\mu_A = 0.2$ $\sigma =$ | 0.008 (c1) | 0.01 (c2) | 0.016 (c3) | 0.024 (c4) | 0.032 (c5) | 0.04 (c6) | 0.08 (c7) |

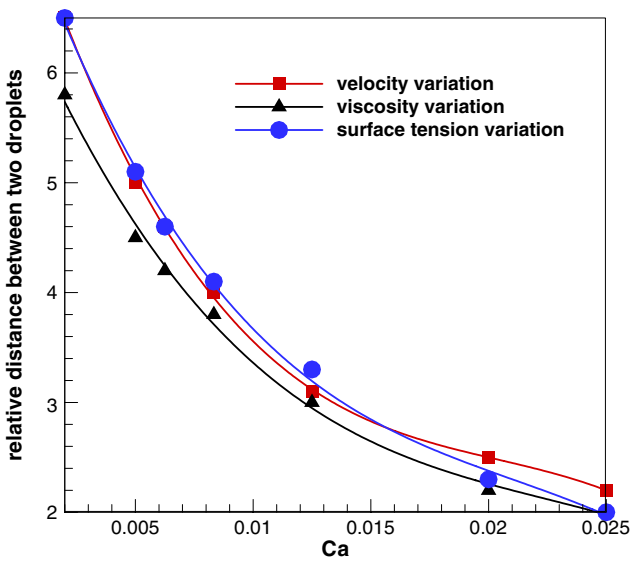


Figure 9. The relative distance between two neighboring droplets at different *Ca* with adjustable parameters $u_A, \mu_A, \sigma$ (refer Table I for the detailed parameter variations).

results in an increase in the distance between two neighboring droplets and an increase in the droplet size.

Figure 9 shows the plot of *Ca* against the relative distance (dividing by the width of the main channel) between two neighboring droplets. The value of *Ca* is changed by adjusting one of the parameters ($u_A, \mu_A, \sigma$ representing each line, respectively) that comprise *Ca*, while the other two are fixed. From Figure 9, it can be seen that the three lines are close to superposition. Again, it proves that the flow mode is decided by *Ca* to a large extent under the current conditions. At the same time, it is noticeable that the lines for velocity and surface tension variations diverge



DOI: 10.1002/fld

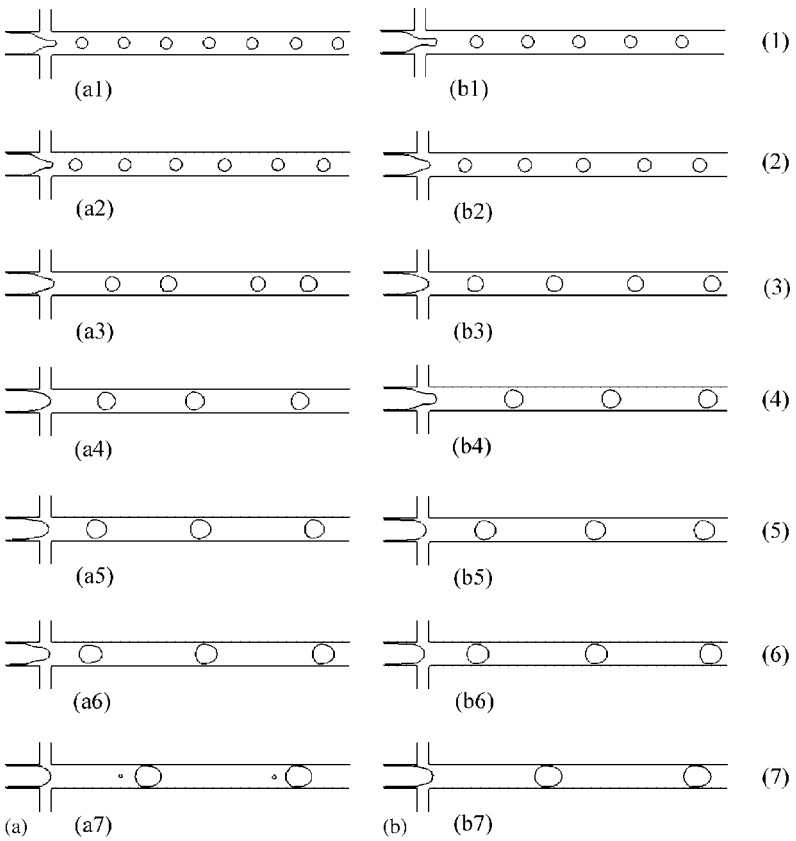


Figure 10. The flow patterns for various *Ca* (each row has same *Ca*) with two different *We* (column (a) for 0.0075, column (b) for 0.0025) (refer Table II for detailed conditions).

from that of viscosity slightly. This may be because another dimensionless Weber number also influences the flow simultaneously although its effect is much smaller under the current conditions. Compared with *Ca*, for the parameters $u_A$, $\mu_A$ and $\sigma$, only $u_A$ and $\sigma$ appear in *We* (Equation (29)). This may provide an explanation for the divergence between the lines of viscosity and the other two. In addition, at large *Ca*, a divergence also appears between the lines of velocity and surface tension variations. This is because of the squared term of velocity, which gives a much larger contribution to *We* compared with surface tension. It is expected that for very large velocities, except for *Ca*, the flow field may also be influenced by *We*. Next, we will test this assertion by simulations.

Figure 10 shows the flow patterns for different *We* ($We=0.0075$, $u_A=0.003$ for column (a); $We=0.0025$, $u_A=0.001$ for column (b)) under various *Ca* for each row. To study the influence of *We* under large inlet velocities, viscosity is used to adjust the *Ca* because it is not included in *We*. Detailed conditions are listed in Table II. From Figure 10, it is found that for small *Ca* ($Ca<0.00833$, rows 4–7), the flow patterns are the same for different *We*, as shown in columns (a) and (b). This is due to the relatively larger influence of *Ca* on the flow. However, with the increase in *Ca* ($Ca>0.0083$, rows 1–3), *We* may share an influence together with *Ca* for the larger



DOI: 10.1002/fld

Table II. Corresponding parameters for Figures 10 and 11.

| | *Ca* | | | | | | |
|---|---|---|---|---|---|---|---|
| Parameters | 0.025 (1) | 0.02 (2) | 0.0125 (3) | 0.00833 (4) | 0.00625 (5) | 0.005 (6) | 0.002 (7) |
| $u_A=0.003$ $\mu_A=$ $\sigma=0.024$ $We=0.0075$ | 0.2 (a1) | 0.16 (a2) | 0.1 (a3) | 0.0667 (a4) | 0.05 (a5) | 0.04 (a6) | 0.02 (a7) |
| $u_A=0.001$ $\mu_A=$ $\sigma=0.008$ $We=0.0025$ | 0.2 (b1) | 0.16 (b2) | 0.1 (b3) | 0.0667 (b4) | 0.05 (b5) | 0.04 (b6) | 0.02 (b7) |

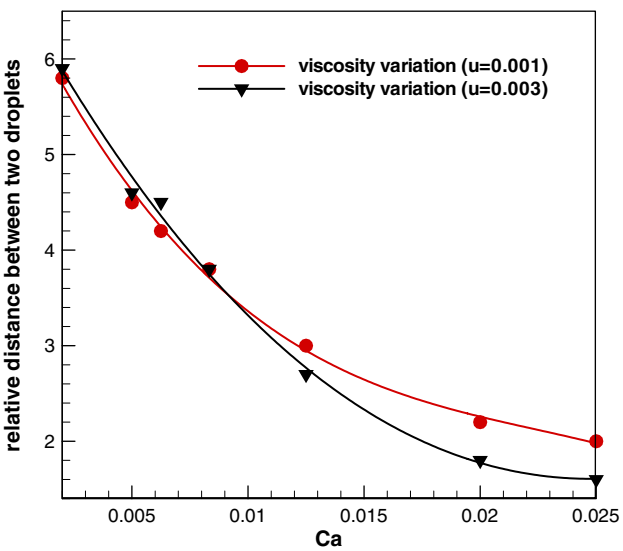


Figure 11. The relative distance between two neighboring droplet at different *Ca* with adjustable parameters $\mu_A$, u representing $u_A$ in the figure caption (refer Table II for the detailed parameter variations).

inlet velocity case (column (a) $We=0.0075$) and much smaller droplets generated (comparing (a1) and (b1)). For the corresponding case of small velocity (column (b) $We=0.0025$), the flow pattern still seems to be dominated by *Ca* only. Besides, in Figure 10 (a3) and (a7), the droplets are formed in pairs in our simulations. At $Ca=0.0125$ (a3), the droplets in each pair have the same size. However, the size of the droplets in the pairs are quite different for $Ca=0.002$ (a7). The generation of binary droplets may result because the flow may be near a type of critical point. In addition, for the case of a small *Ca* (a7), the surface tension effect is very strong compared with the viscosity effect ($\mu=0.02$). Under such conditions, simulations may enlarge some numerical error or unstable factors and generate very uneven droplets.

Figure 11 shows the plot of relative distance between two neighboring droplets (dividing by the width of the main channel) *versus* *Ca* for different inlet velocities. At small *Ca* ($Ca<0.00833$),



DOI: 10.1002/fld

the two lines almost superpose. This is because the influence of *We* is much smaller compared with that of *Ca*. When *Ca* is larger than 0.00833, the results become different between the cases of $u_A = 0.001$ and 0.003. This difference becomes larger and larger with increasing *Ca*. It is because in the large velocity case, the influence of *We* is large enough and comparable to that of *Ca*.

## 5. CONCLUSIONS

In the present work, we proposed a new LBM model. The utility of the current method for easily and accurately simulating multiphase flows was demonstrated by the simulations of static bubble flow. A 2-D simulation was carried out on the immiscible two-phase flow in a cross-junction microchannel using this model. The influence of two dimensionless numbers, *Ca* and *We*, were studied. The following conclusions were drawn:

(1) The present method has the advantage of decreasing the spurious velocities and artificial side effect around the interface over some existing models.
(2) In the simulation of two-phase flow in a cross-junction microchannel, the flow pattern and velocity field agree well with the experimental results in a qualitative analysis.
(3) The flow patterns are decided almost entirely by *Ca* for small inlet velocities.
(4) When the inlet velocity is large, the flow mode is not decided only by *Ca* and the influence of the *We* is also significant because of the squared velocity term.

## REFERENCES

1. Doku GN, Verboom W, Reinhoudt DN, Berg AVD. On-microchip multiphase chemistry—a review of microreactor design principles and reagent contacting modes. *Tetrahedron* 2005; **61**:2733–2742.
2. Hirt CW, Nichols BD. Volume of fluid (VOF) method for the dynamics of free boundary. *Journal of Computational Physics* 1981; **39**:201–225.
3. Sussman M, Smereka P, Osher S. A level set approach for computing solutions to incompressible two-phase flow. *Journal of Computational Physics* 1994; **114**:146–159.
4. Tryggvason G, Bunner B *et al*. A front-tracking method for the computations of multiphase flow. *Journal of Computational Physics* 2001; **169**:708–759.
5. Liu J, Koshizuka S, Oka Y. A hybrid particle-mesh method for viscous, incompressible, multiphase flows. *Journal of Computational Physics* 2005; **202**:65–93.
6. Yabe T, Xiao F, Utsumi T. The constrained interpolation profile method for multiphase analysis. *Journal of Computational Physics* 2001; **169**:556–593.
7. Chen S, Doolen GD. Lattice Boltzmann method for fluid flows. *Annual Reviews of Fluid Mechanics* 1998; **30**:329–364.
8. Gunstensen AK, Rothman DH, Zaleski S, Zanetti G. Lattice Boltzmann model of immiscible fluids. *Physical Review A* 1991; **43**:4320–4327.
9. Lishchuk SV, Care CM, Halliday I. Lattice Boltzmann algorithm for surface tension with greatly reduced microcurrents. *Physical Review E* 2003; **67**:0367011–0367015.
10. Latva-Kokko M, Rothman DH. Diffusion properties of gradient-based lattice Boltzmann models of immiscible fluids. *Physical Review E* 2005; **71**:0567021–0567028.
11. Rothman DH, Zaleski S. *Lattice Gas Cellular Automata*. Cambridge University Press: Cambridge, 1997.
12. Brackbill JU, Kothe DB, Zemach C. A continuum method for modeling surface tension. *Journal of Computational Physics* 1992; **100**:335–354.
13. Succi S. *The Lattice Boltzmann Equation for Fluid Mechanics and Beyond*. Oxford University Press, Clarendon Press: Oxford, 2001.
14. Dupin MM, Halliday I, Care CM. Simulation of a microfluidic flow-focusing device. *Physical Review E* 2006; **73**:055701–055704.



DOI: 10.1002/fld